# Imaging of the topside ionosphere using GNSS slant TEC obtained from LEO satellites

**Lucas Schreiter[1,2], Andreas Brack[2], Benjamin Männel[2], Harald Schuh[1,2], Daniel Arnold[3], Adrian Jäggi[3]**

[1]Technical University of Berlin, Berlin, Germany
[2]Helmholtz Centre Potsdam - GFZ German Research Centre for Geosciences, Potsdam, Germany
[3]University of Bern, Bern, Switzerland

**Key Points:**

- Slant TEC from 27 LEO satellites, including Spire LEMURE CubeSats, is used to model the electron density in the topside ionosphere.
- Excellent agreement is achieved in validating against in situ electron density measured by Swarm and DMSP and vTEC from Jason-3.
- Comparison to up-to-date artificial neuronal network models is performed.

Corresponding author: Lucas Schreiter, schreit@gfz-potsdam.de

**Abstract**

Satellites with dual-frequency Global Navigation Satellite Systems (GNSS) receivers can measure integrated electron density, known as slant Total Electron Content (sTEC), between the receiver and transmitter. Precise relative variations of sTEC are achievable using phase measurements on L1 and L2 frequencies, yielding around 0.1 TECU or better. However, CubeSats like Spire LEMUR, with simpler setups and code noise in the order of several meters, face limitations in absolute accuracy. Their relative accuracy, determined by phase observations, remains in the range of 0.1-0.3 TECU. With a substantial number of observations and comprehensive coverage of lines of sight between Low Earth Orbit (LEO) and GNSS satellites, global electron density can be reconstructed from sTEC measurements. Utilizing 27 satellites from various missions, including Swarm, GRACE-FO, Jason-3, Sentinel 1/2/3, COSMIC-2, and Spire CubeSats, a cubic B-spline expansion in magnetic latitude, magnetic local time, and altitude is employed to model the logarithmic electron density. Hourly snapshots of the three-dimensional electron density are generated, adjusting the model parameters through non-linear least-squares based on sTEC observations. Results demonstrate that Spire significantly enhances estimates, showcasing exceptional agreement with in situ observations from Swarm and Defense Meteorological Satellite Program (DMSP). The model outperforms contemporary climatological models, such as International Reference Ionosphere (IRI)-2020 and the neural network-based NET model. Validation efforts include comparisons with ground-based slant TEC measurements, space-based vertical TEC from Jason-3 altimetry, and global TEC maps from the Center for Orbit Determination in Europe (CODE) and the German Research Center for Geosciences (GFZ).

## 1 Introduction

The ionosphere, consisting of weakly ionized plasma, is categorized into layers based on chemical composition. The dynamics of this plasma are primarily influenced by Earth's magnetic field. At higher altitudes, the ionosphere transits into the plasmasphere—a plasma torus with electron densities ranging from 10 to $10^5$ e/cm$^{-3}$ (at low L values, i.e., the apex of the magnetic field line in Earth radiis), closely linked to the magnetic field lines (Ripoll et al., 2023). Ionized plasma affects radio waves due to its dispersive nature, causing delays in code measurements and advancements in phase measurements, proportional to $1/f^2$ for carrier frequency $f$. Dual-frequency measurements effectively eliminate more than 90% of the range error through a linear combination, aiding in estimating the integrated electron content (sTEC). Single-frequency users require external assistance for slant TEC information.

Ground-based receiver networks routinely monitor the ionosphere using GNSS. In operational procedures, slant TEC measurements from ground stations are mapped to vertical TEC using a mapping function. Spherical harmonics model the mapped vertical TEC, generating global TEC maps (Schaer, 2011; Brack et al., 2021). These maps assume all contributing electrons are compressed in a thin shell at 350 km to 450 km height, suitable for ground-based observations. However, this assumption falters for Low Earth Orbit (LEO) satellites, especially CubeSats, where sensitivity to variations in peak height, altitude profile, and spatial gradients is pronounced. Approaches such as ionospheric tomography, data assimilation, and plasmasphere estimation from LEO satellite slant TEC observations address this challenge.

In recent years, the surge in LEO satellites, including science missions like Swarm, Sentinel, GRACE-FO, COSMIC-2, Jason-3, and commercial CubeSats like Spire's LEMUR, equipped with dual-frequency GNSS receivers, has been notable. This study employs 27 LEO satellites, presenting a unique opportunity to directly reconstruct electron density in the topside ionosphere using slant TEC observations. Temporally, the resolution is 1h, with spatial resolution at 3° in magnetic latitude and $0.5h$ in magnetic local time. Altitude is

represented by 15 non-uniformly spaced basis functions between 100 km and 500 km, with restricted variation above 3000 km to GPS altitude ($\tilde{2}$0000 km). Despite limited coverage due to satellite tracks, especially during 3/15 LT, the study demonstrates robust reconstruction.

Slant TEC is calculated from observations collected by the Precise Orbit Determination (POD) antenna on the mentioned satellites. The procedure follows established methodologies, with receiver code biases adjusted during model estimation. Three-dimensional electron density maps are computed based on relative slant TEC, validated against in situ measurements from Swarm, DMSP, and GRACE-FO, as well as integral measurements from Jason-3 altimeter and ground-based TEC maps.

The paper is structured as follows: Section 2 outlines slant TEC computation methods and limitations, while Section 3 introduces the three-dimensional model and its estimation. Section 4 discusses results, emphasizing internal consistency, and Section 5 provides external validation using Langmuir Probes, Jason-3, and ground stations. Section 6 delves into the discussion of the results, focusing on small satellites, with Section 7 presenting conclusions.

## 2 Slant TEC computation

For certain satellite missions, such as Swarm (operational data from ESA, DISC (2017)), GRACE-FO (provided by GFZ within the TIRO project, Schreiter et al. (2023)), and COSMIC-2 (provided by UCAR, UCAR (2019)), slant TEC data is already available. To ensure consistency across all missions, including identical criteria, methods, and data structure, slant TEC is computed again for every mission in this study. The processing methodology agrees with the procedures used in TIRO (Schreiter et al., 2023; Noja et al., 2013) and UCAR (Yue et al., 2011).

Relative slant TEC is derived from dual-frequency code or phase measurements using the formula:

$$rsTEC = L_1 - L_2 \tag{1}$$

The processing is centered on geometry-free linear combinations, $P_4 = P_2 - P_1$ of code observations, and $L_4 = L_1 - L_2$ of phase observations. The opposite sign accounts for opposed ionospheric effects in code and phase measurements. Aside from differential code biases for $P_4$ and ambiguity parameters and phase biases for $L_4$, these are proportional to slant TEC. Phase observations undergo correction for phase wind-up using nominal attitude law for GPS satellites (Montenbruck et al., 2015), coupled with attitude information from the LEO satellites. The formulas from Wu et al. (1992) and Beyerle (2009) are then applied to compute phase wind-up corrections and subsequently applied to carrier phase measurements.

Additionally, the Melbourne-Wuebbena (MW) linear combination is utilized for data screening:

$$L_{MW} = \frac{1}{f_1 - f_2}(f_1 L_1 - f_2 L_2) - \frac{1}{f_1 + f_2}(f_1 P_1 + f_2 P_2), \tag{2}$$

where $f_1$ and $f_2$ are the carrier frequencies for $L_1$ and $L_2$. This is employed for screening purposes, with screening parameters shown in Tab. 1. The input requirements include the receiver RINEX file, the LEO satellite's attitude, and the LEO orbit provided as SP3 files. GNSS orbits and code biases from the Center for Orbit Determination in Europe (CODE, (Dach et al., 2020)) are also necessary. The processing begins with loading RINEX observation data, merging it with orbit and attitude information for both, LEO and GNSS. Rotations from the inertial frame to the spacecraft body-fixed frame and eventually to the antenna reference frame are applied (see Tab. 2). Phase wind-up corrections are then applied to the phase observations. Cleaning involves a combination of MW-based screening similar to Cai et al. (2013), L4 screening (epoch differences), and checking the completeness of observation sets (minimum $P_1$, $P_2$, $L_1$, $L_2$).

| Satellite | MW window (s) | max. gap (s) | MW max. std. in window (m) | MW max. jump (m) | min. arc length (#obs.) | max. jump L4 (m/s) | max. jump MP LC (m/s) | SNR limit (dB-Hz) |
|---|---|---|---|---|---|---|---|---|
| Default | 50.5 | 10.5 | 0.2 | 0.43 | 5 | 0.5 | 0.2 | 23.5 |
| Jason-3 | 50.5 | 10.5 | 0.2 | 0.43 | 5 | 0.5 | 0.2 | - |
| COSMIC-2 | 50.5 | 10.5 | 0.2 | 0.43 | 5 | 1.0 | 0.2 | 23.5 |
| Spire | 50.5 | 10.5 | 2.0 | 1.29 | 5 | 0.5 | 5.0 | 23.5 |

**Table 1.** Screening parameters for the different satellite missions used. In the case of Jason-3, the SNR is not reported in the RINEX file. RINEX observation files are sampled to 0.1 Hz in advance.

Due to Spire's relatively large code noise, the Melbourne-Wuebbena based screening is relaxed for Spire (see Tab. 1). For COSMIC-2, screening based on the geometry-free linear combination is relaxed due to high signal dynamics when sounding with negative elevations.

Observations are corrected for GNSS code biases, and GNSS satellite positions are interpolated to the observation eoochs. Elevation and azimuth in the antenna frame are computed based on the satellite attitude file. For each code observation, the multipath linear combination is computed and binned into 1° bins of elevation and azimuth, stacked over a longer period (here one month) to mitigate noise (Montenbruck & Kroes, 2003). Multipath corrections are applied to code observations, and code leveling is performed for each continuous phase arc. A phase arc is considered continuous as long as the ambiguity parameter is unchanged. This assumption holds under conditions of no tracking gaps, Melbourne-Wuebbena linear combination having no jumps larger than 43 cm (half cycle) with 10s boxcar smoothing, and no large jumps in the geometry-free linear combination ($> 0.5$ m/s) (see Tab. 1).

The Melbourne-Wuebbena linear combination condition is relaxed for Spire satellites due to large code noise (129 cm instead of 43 cm, with 50-second smoothing). For COSMIC-2, the third condition is relaxed due to the fast-increasing slant TEC when the elevation becomes negative ($1m/s$ instead of $0.5m/s$). After code leveling, the receiver-specific P1-P2 bias is estimated using an approach presented by Yue et al. (2011), adjusting the receiver bias such that simultaneously observed slant TEC observations are equal after applying a mapping function. The slab-layer mapping function from Foelsche and Kirchengast (2002) with a slab thickness of 400 km is selected for this study, consistent with DISC (2017). Note that these leveling approaches are considered initial guesses in this work, and code leveling depends on code observation quality, with phase observations offering better relative accuracy.

The arc decomposition is stored in the derived TEC file and reused for the model adjustment.

## 3 Model estimation

The model represents the logarithmic electron density ($N_e$) using cubic B-splines in magnetic latitude ($B^{mlat}$, with $n_{mlat}$ basis functions), magnetic local time ($B^{mlt}$, with $n_{mlt}$ basis functions), and altitude ($B^{alt}$, with $n_{alt}$ basis functions):

$$log_{10}N_e = \sum_{i=1}^{n_{mlat}} \sum_{j=1}^{n_{mlt}} \sum_{k=1}^{n_{alt}} B_i^{mlat} \cdot B_j^{mlt} \cdot B_k^{alt}. \quad (3)$$

Magnetic latitude and magnetic local time are based on Apex coordinates (Richmond, 1995; Emmert et al., 2010). The logarithmic representation is chosen because classical approaches

| Satellite | Antenna roll (degrees) | Antenna pitch (degrees) | Antenna yaw (degrees) |
|---|---|---|---|
| Swarm | 180 | 0 | 180 |
| GRACE-FO | 180 | 0 | 0 |
| Jason-3 | 180 | -15 | 0 |
| Sentinel 1 | 204.9 | 14.64 | 0 |
| Sentinel 2 | 0 | -165 | 0 |
| Sentinel 3 | 180 | 0 | 0 |
| COSMIC-2 | 180 | +/-20 | 0 |
| Spire | 0 | 0 | 0 |

**Table 2.** Antenna rotations used to rotate from satellite body fixed frame to antenna reference frame. In the case of COSMIC-2 +20 is used for antenna 1 and -20 for antenna 2.

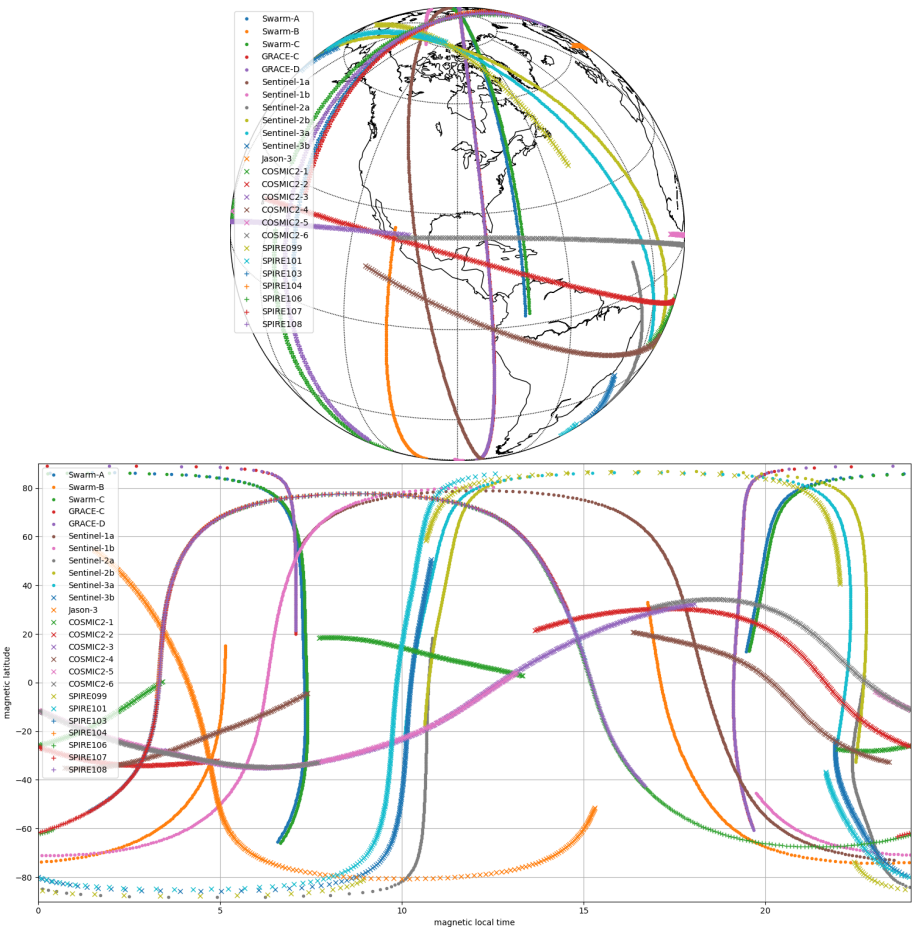


**Figure 1.** Positions of the LEO satellites used in the geodetic frame (top) and in geomagnetic latitude and local time (bottom). The time span used is just one hour (May, 2 nd, 00:00-01:00 UTC)

like Chapman- or Epstein-Layer (or also Varychap) assume linear or quadratic decay in altitude for the logarithmic electron density (Chapman, 1931; Rawer, 1983; Nsumei et al., 2012; Smirnov et al., 2023; Prol et al., 2021). The cubic B-splines allow covering linear or quadratic decay, making them a generalization of layer function assumptions. To capture higher variability in near-peak altitudes, the knot vector of the B-splines is selected with smaller spacing between 200 km and 500 km. Larger altitudes, being less well-covered, have increased spacing. In magnetic latitude, a cubic B-spline basis with equal spacing and padding at the poles is chosen. In magnetic local time, the B-spline basis has periodic boundary conditions. The single-dimension basis functions generate a three-dimensional basis using the tensor product.

Integration of electron density along the line of sight is performed using Gauss-Legendre quadrature. Given most variability in the bottom side, ten support points are computed along the line of sight below 3000 km. To account for plasmaspheric TEC contribution, integration from 3000 km to GPS satellite altitude is performed using five support points. The integration is a linear operator expressed using a matrix LL of dimension $(n, 15 \cdot n)$, where $n$ is the number of slant TEC observations. The logarithmic electron density at the support points is derived from the model parameters using the design matrix $D$, with entries being the values of the basis functions at the support points. Consequently, the dimension of $L$ is $(15 \cdot n, npar)$ where $npar$ is the number of model parameters.

It is important to note that the selection of basis functions significantly impacts computational effort. B-splines are chosen for their compact support, resulting in sparse design matrix $D$. This sparsity also holds for matrix $L$, where only 15 entries deviate from zero in each row. With $y$ as the vector containing observed sTEC values in TECU and $x$ containing the model parameters, the minimization problem is written as:

$$\|L \cdot \exp(D \cdot x)10^9/10^{16} - y\| \rightarrow min. \tag{4}$$

The factor $10^9/10^{16}$ accounts for the electron density in $cm^{-3}$ and TECU in $10^{16}e/m^2$. As leveling uncertainty of TEC values is high compared to the relative accuracy of slant TEC, one offset parameter is added to each continuous phase arc. With $O$ as the matrix linking offsets to slant TEC observations and $x_o$ containing the offsets (in TECU), the minimization problem is:

$$\|L \cdot \exp(D \cdot x)1e9/1e16 + O \cdot x_o - y\| \rightarrow min. \tag{5}$$

The matrix $O$ is sparse. Some basic functions are not well-observed, especially in polar regions where the grid in magnetic latitude and magnetic local time is less spaced. To account for this situartion, constraints are weighted with the inverse cosine of magnetic latitude, suppressing large variations in polar regions. The altitudinal expansion is unconstrained. Constraints are applied using Tikhonov regularization:

$$\|L \cdot \exp(D \cdot x)1e9/1e16 + O \cdot x_o - y\| + \lambda\|C \cdot x\| \rightarrow min. \tag{6}$$

It is crucial to note that only parameters describing the electron density are constrained, while estimated offsets remain unconstrained. An initial guess for electron density parameters is made by estimating $x$ from the IRI-2020 model using the cor2 topside with plasmasphere extension. The a priori estimate for $x_o$ is 0 (vector) since a rough estimate is performed in the slant TEC computation. Model adjustment is done using non-linear least-squares adjustment. The constraining parameter $\lambda$ is fixed, and selected using the L-curve criterion.

## 4 Results

The electron density is adjusted to make the modeled slant TEC match the observed slant TEC (excluding arc-wise offsets). The observed slant TEC, modeled TEC, and TEC extracted from the IRI-2020 model with cor2 topside are shown in Fig. 2. The model parametrization can reproduce the elevation-dependent characteristics of the measured slant

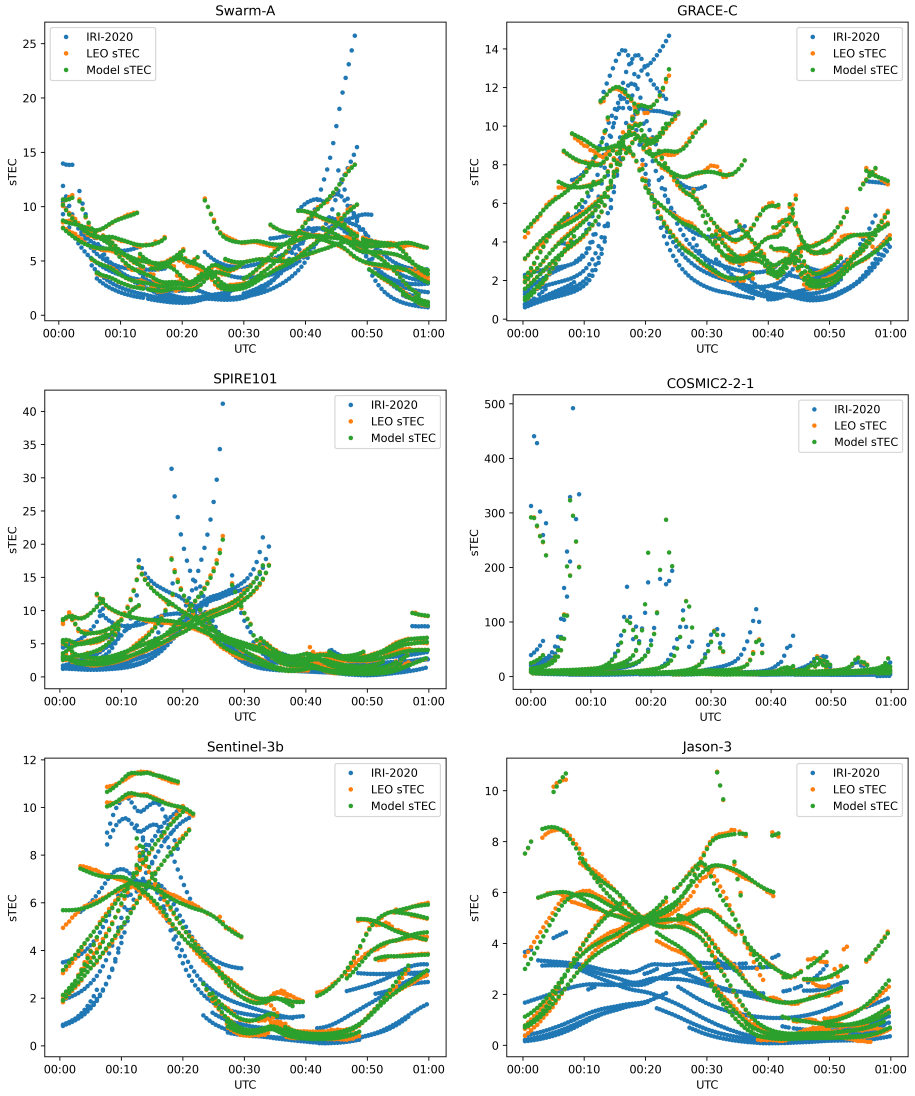


**Figure 2.** Slant TEC values for Swarm A, GRACE-C, Spire-101, COSMIC-2 (Antenna 1), Sentinel-3B, and Jason-3. The slant TEC values are computed from IRI-2020 using NeQuick as topside (blue), From the model after model adjustment (green), and observed slant TEC with receiver bias adjusted (orange). Large values for COSMIC-2 occur due to occultation measurements.

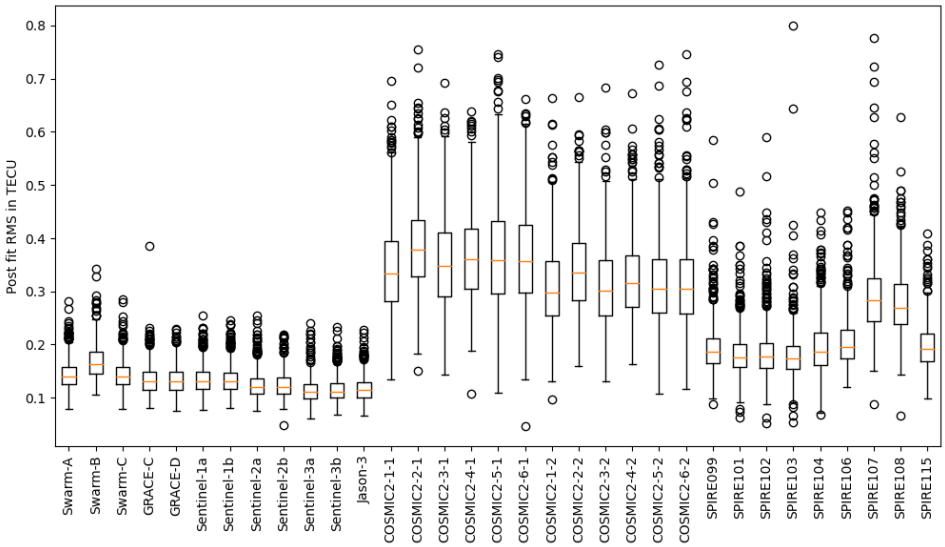


**Figure 3.** Post-fit RMS for the satellite missions used for the reconstruction. The last number for the COSMIC-2 satellites references the antenna number.

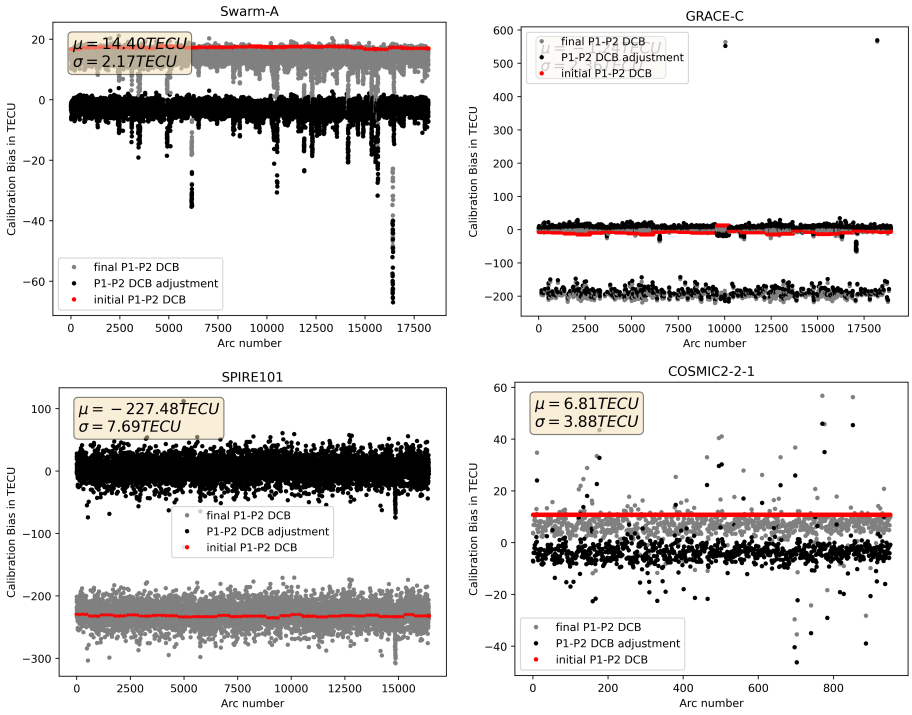


**Figure 4.** Estimated differential code biases for the receiver for Swarm, GRACE-C, Spire101, and COSMIC-2 (2 Antenna 1).

TEC (i.e., a strong increase with low elevation), and the model TEC values agree with the observed slant TEC within less than 1 TECU. Additionally, the agreement with the IRI-derived TEC is typically within 3 TECU for low-flying satellites like Swarm and GRACE-FO, except at the end of observational arcs coinciding with low elevations. The agreement between sTEC observed by Jason-3 is not as well captured by the IRI-2020 model, indicating a significant underestimation of ionospheric gradients by IRI-2020. This suggests that a generalization of the profile functions could be essential to better describe the transition region between the ionosphere and plasmasphere.

Hourly ionospheric electron density maps are computed for a full month (May 2020). The post-fit Root Mean Square (RMS) between observation and model is approximately between 0.2 and 0.3 TECU (see Fig. 3) and higher for COSMIC-2 due to occultation measurements. Spire satellites lead to higher values due to increased observational noise. Compared to Swarm, the RMS for Spire is about three times higher (consistent with the results from POD, (Arnold et al., 2023)). However, the reconstruction still benefits from the improved observational geometry, as shown in the validation section.

The errors introduced by code leveling are typically in the range of a few TECU. Especially for short observational arcs, this error may become large, and a second uncertainty is the receiver-specific code bias. Both are handled by estimating arc-wise DCBs during the adjustment. Selected DCBs are shown in Fig. 4. For Swarm, the arc-wise DCBs show a scatter of about 2 TECU, as expected. Larger jumps of several hundred TECU are observed for GRACE-FO C, affected by flex-power tracking issues (Schreiter et al., 2023). However, the phase observation seems unaffected. For Spire, a much larger scatter of nearly 8 TECU is seen due to noisier code observations and CubeSat limitations. This noise also indicates that classical code leveling for TEC computation would not exploit the potential of the GNSS receiver. The noise for COSMIC-2, that is likely caused by the occultation measurements and larger signal dynamics, is larger than for Swarm but still much smaller than for Spire.

## 5 Validation

### 5.1 Ground-based TEC

The derived electron density is validated against TEC and electron density observations as well as established models. First, we validate against ground-based observations using IGS stations: Zimmerwald in Switzerland (mid-latitude, ZIM200CHE, $46.877°N, 7.465°E$), Cap Verde in Spain (CPVG00CPV,$16.732°N, 22.935°W$), Le Lamentin in Martinique (LMMF00MTQ, $14.595°N, 60.996°W$), and Accra in Ghana (ACRG00GHA, $5.641°N, 0.207°W$) (near the magnetic equator). The modeled slant TEC is obtained by integrating the model from the lowest modeled altitude (100 km) up to the GPS satellite position. For the bottom side (below 450 km), data mostly rely on COSMIC-2 data and occasionally Spire POD with negative elevations. To mitigate outliers, a Butterworth low-pass filter is applied to the model coefficients. The comparison is performed against the CODE TEC model as a reference.

The observed standard deviation is near 1.5 TECU for Zimmerwald for both the CODE TEC map and the model, with a slight degradation in the model during the afternoon. For Cap Verde, the standard deviations for the model and the TEC map are similar around 2 TECU, in contrast to IRI, which shows significantly higher values up to 6-8 TECU. For Accra, the model leads to smaller standard deviations than the TEC map, with a degradation in the early afternoon, an area not well covered by the satellites. Similar behavior is noticeable for Le Lamentin.

### 5.2 Vertical TEC from Jason-3 Altimeter

Vertical Total Electron Content (vTEC) derived from altimeter measurements over the oceans is used in this study, specifically from Jason-3. The satellite orbits the Earth with

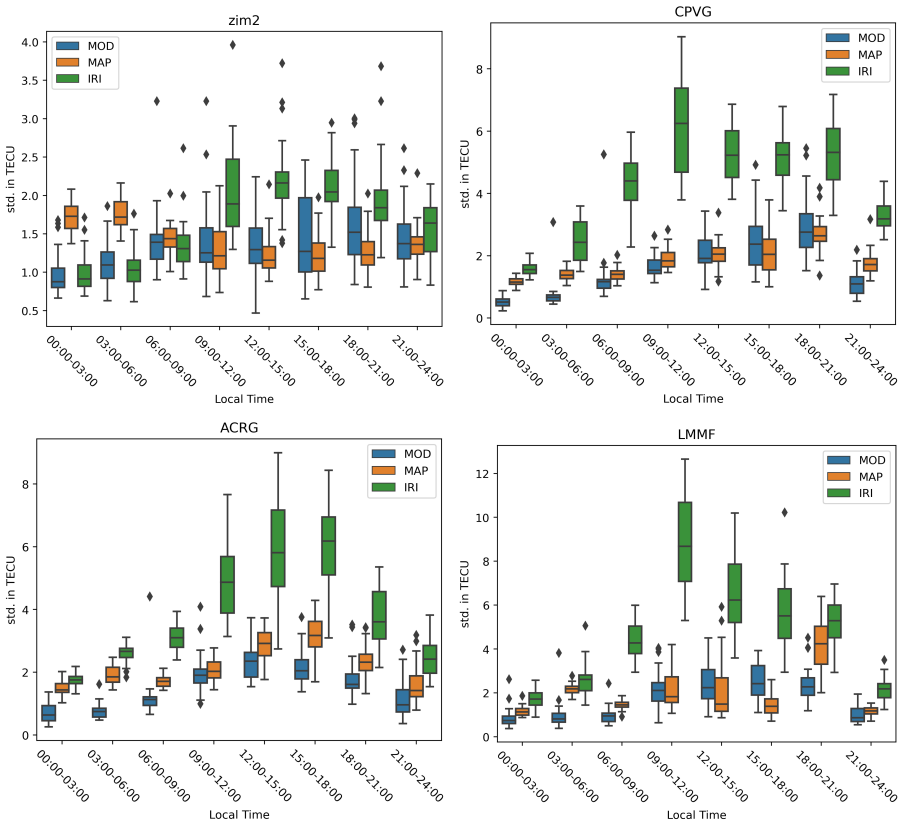


**Figure 5.** Standard deviation binned in local time for the selected ground stations

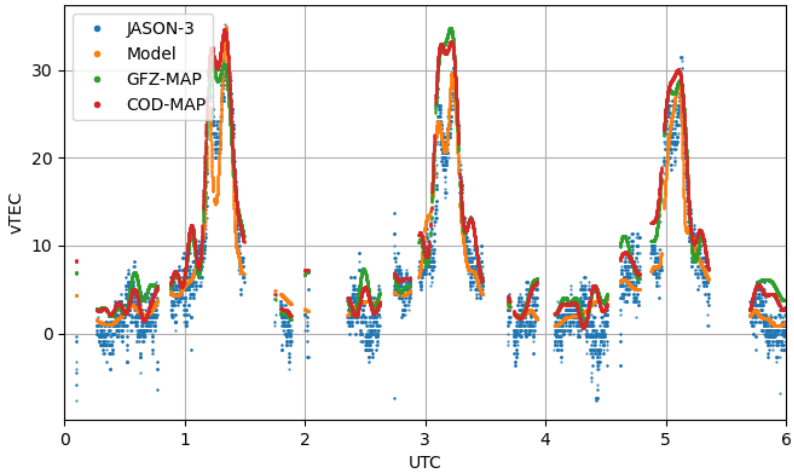


**Figure 6.** Jason-3 vertical TEC obtained from altimeter compared to vertical TEC computed from the model (orange), GFZ TEC maps (green), and CODE TEC maps (red)

an inclination of 66° at an altitude of around 1300 km. Due to the measurement principle and its altitude, it misses the contribution of the electron density between the satellite orbit height and GNSS altitude to the vertical TEC between ground and GNSS satellites. The three-dimensional electron density model is capable of separating the TEC below and above a given altitude, which is a few TECUs. The comparison in Fig. 6 shows Jason-3 vTEC obtained from altimetry compared to the vertical TEC computed from the model (in orange), GFZ TEC maps (in green), and CODE TEC maps (in red). The model TEC is derived through numerical integration from the ground to Jason-3 altitude. The TEC maps from CODE and GFZ are not scaled to remove the TEC contributions originating from 1300 km upwards.

The equatorial double peak is better reproduced using the reconstruction compared to the TEC maps. The TEC maps use spherical harmonics up to degree/order 15, resulting in a 12° resolution in latitude, while the B-spline approach is selected with a 3° resolution in latitude. Over the full day, the Root Mean Square (RMS) between the vertical TEC from Jason-3 and the model, CODE, and GFZ TEC is 2.46 TECU, 2.72 TECU, and 2.83 TECU, respectively, which is close to the noise level of the Jason-3 TEC observations. If a boxcar smoothing with a 60-second window is used to mitigate high-frequency scatter in Jason-3 vTEC, the RMS drops to 2.08 TECU (model), 2.49 TECU (GFZ), and 2.37 TECU (CODE). In case the electron density is integrated only to Jason-3 altitude (1300 km), the model RMS increases to 2.24 TECU, treating the TEC maps and the model identically.

### 5.3 Electron Density

The electron density is adjusted based on in situ measurements from Swarm and DMSP. The electron densities from Swarm, which operates at altitudes of 460 km (A/C) and 510 km (B), and from DMSP, which orbits between 850 km and 880 km, are adjusted due to the observed overestimation of the electron density (Pakhotin et al., 2022; Catapano et al., 2022). The adjustment is crucial to improve the accuracy of the electron density profiles derived from the three-dimensional model.

Swarm electron densities are computed from ion admittance, assuming a pure oxygen atmosphere and single-charged ions. The ion density ($N_i$) is calculated using the formula:

$$N_i = \frac{d_s v_s m_s}{2e^2 \pi r_p^2}, \tag{7}$$

where $N_i$ is the ion density, $d_s$ is the ion admittance, $v_s$ is the plasma ram speed, $m_s$ is the effective ion mass, $e$ is the elementary charge, and $r_p$ is the probe spherical radius. The effective ion mass is considered 16 atomic mass units (AMU) for a pure oxygen atmosphere.

To account for variations in the effective ion mass during nighttime or at higher altitudes (Swarm B), where light ions like $He^+$ and $H^+$ contribute, the effective ion mass is adjusted. The adjustment involves extracting the ion composition from the IRI-2020 model, specifically using the ion composition model from Truhlik et al. (2015). The effective electron density extracted from the model ($m_{eff}^{mod}$) is then used to adjust the electron density obtained from Swarm, multiplying it by $m_{eff}^{mod}/16$. This adjustment is only applied to Swarm as there is no information available on the electron retrieval algorithm from DMSP.

The study includes the use of "in situ" electron density data obtained from the GRACE-FO satellites. While it is noted that the GRACE-FO K-Band instrument provides a smoothed average of the electron density between the two satellites rather than a direct in situ measurement, it serves as a valuable dataset for comparison.

In Fig. 7, a comparison is presented for the period 00:00-04:00 UTC on the 2nd of May 2020, featuring data from Swarm A, Swarm B, DMSP-F18, and GRACE-FO. Notably, the IRI-2020 model exhibits a pronounced overestimation near sunrise, particularly evident in Swarm A. In contrast, both the NET model and the reconstructions show a more accurate representation without the observed overestimation. The same overestimation pattern is seen for GRACE-FO, emphasizing the likelihood of it being a local time-dependent feature.

For Swarm B, where electron density adjustments were applied, all models demonstrated excellent performance. Without adjustment, Swarm B would exhibit a significant peak in electron density on the night side. The reconstructions effectively capture the measurements from DMSP, although IRI and NET fail to capture the peak amplitude, particularly notable in the NET model due to features related to the Epstein layer and the adjustment process based on radio occultations that do not include density values above 800 km.

The overall performance for the full day is summarized in Fig. 8. The reconstructions showcase their ability to capture variations in in situ measured electron densities, with a correlation coefficient of 0.92. When Spire is included in the model generation, the correlation increases to 0.95. Particularly noteworthy is the nearly met correlation for the NET model with Swarm satellites, while for higher flying DMSP satellites, IRI performs better. The Root Mean Squared Error (RMSE) analysis indicates that the error in electron density for the derived model is only around 40% of the error in the IRI model. This emphasizes the improved accuracy and performance of the NET model, especially for Swarm, while its effectiveness drops with altitude.

## 6 Discussion

Apart from classical large scientific satellites, we use also a fleet of CubeSats in this study. The utilization of CubeSats, particularly the Spire satellites in this study, raises two key questions:

1. Benefit of Spire Satellites in Reconstruction:
   - The impact of Spire satellites on the reconstruction is assessed through validation results. It is observed that the model, which incorporates Spire data, exhibits an

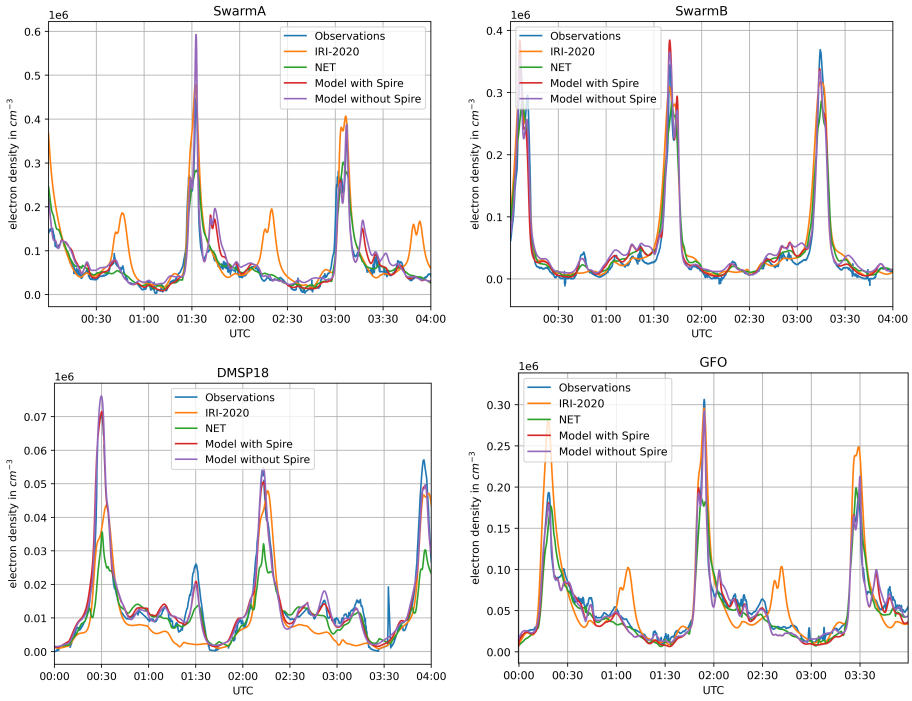


**Figure 7.** Electron density for Swarm A (top left, 07/19 LT), Swarm B (top right, 05/17 LT), DMSP-F18 (bottom left, 05/17 LT) and GRACE-FO (bottom right, 07/19 LT)

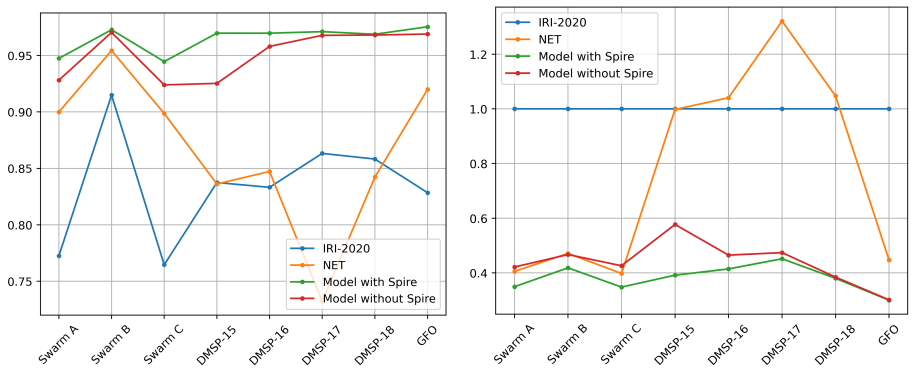


**Figure 8.** Left: Correlation between observed electron density and modeled electron density for the model with, and without Spire compared with IRI and NET. Right: RMSE relative to IRI-2020 for NET, and the model with and without Spire

increase in correlation for all in situ measurements from approximately 0.95 to 0.97. Simultaneously, the error in electron density decreases, measured relative to IRI, from 0.4 to 0.35. This improvement is attributed to the different local times covered by Spire satellites, contributing to densification in magnetic local time and magnetic latitude, thereby enhancing the observation geometry.

2. Data Quality of Spire Satellites:
   - The data from Spire satellites is noted to have significantly increased observation noise compared to other missions. The elevated noise levels are likely a consequence of the CubeSat design, which may limit the payload. Specifically, the code noise for Spire is observed to be near 4m, in contrast to the usual 1m observed on other satellites like Sentinel. The analysis of the standard deviation of arc-wise biases further supports this, with GRACE-FO having a standard deviation of around 2 TECU, while Spire exhibits a higher value of around 7 TECU. This indicates a 3-4 times larger code noise for Spire.
   - The study also evaluates the phase noise, considering the post-fit RMS of relative slant TEC. Spire satellites exhibit a post-fit RMS around 0.2 TECU, while Swarm and GRACE-FO, with similar heights, show a lower post-fit RMS near 0.1 TECU. Despite the higher noise, the study concludes that the additional observations from different local times provided by Spire outweigh the impact of larger noise.
   - It is emphasized that the model used in the reconstruction relies on relative variations in slant TEC based on phase measurements. Although code noise is a concern for TEC derivation using code leveling techniques, the study suggests that for the reconstruction, the limiting factor is phase noise, and the amount of additional observations from other local times compensates for the larger noise from Spire.

In summary, while Spire satellites introduce increased observation noise, their inclusion in the study enhances the overall reconstruction by providing valuable observations from different local times. The benefits of densification and improved observation geometry outweigh the challenges associated with data quality.

## 7 Conclusions

The study successfully reconstructs electron density in the topside ionosphere and plasmasphere using observations from Low Earth Orbit Global Navigation Satellite System (LEO-GNSS). Key findings and conclusions from the study include:

1. Agreement with In Situ Measurements: The reconstructed electron density demonstrates excellent agreement with in situ electron density measurements. The performance surpasses that of climatological models such as IRI-2020 and NET.
2. Validity Range: While the estimation is performed up to 20,000 km, the validity of the reconstruction is suggested up to 5,000 km. Above this altitude, the contribution to slant Total Electron Content (TEC) is deemed negligible, and reliable reconstruction is challenging. Only approximately 1.5 TECU remains above 5,000 km in low and mid-latitudes around noon.
3. Global Coverage Limitations: GNSS satellites, with a revolution time of approximately 11:58 h for GPS, do not provide global coverage similar to LEO satellites within a 1-hour time window. The study notes limitations in reconstructing high altitude regimes on a short time scale due to unequal data sampling of LEO satellites in local time. Future mega constellations may address this limitation.
4. Comparison to Ground-Based TEC: Comparison with ground-based TEC observations reveals that the quality of the reconstruction is affected by the unequal data sampling of LEO satellites in local time. Reasonable agreement within 2 TECU can be achieved for local times between 00 and 12. However, the Root Mean Square (RMS) increases to 2.5 TECU in early afternoon local times (between 12 and 24).

5. Reconstruction over Oceans Using Altimetry Measurements: The study demonstrates the reliable reconstruction of vertical TEC over oceans using altimeter measurements from Jason-3 as a reference. The B-spline basis used in the reconstruction provides a better resolution of the double peak structure near the geomagnetic equator compared to spherical harmonics used in TEC maps.
6. Validation with In Situ Electron Density Measurements: In situ electron density was validated using measurements from Swarm, DMSP, and GRACE-FO. The study shows a correlation of 0.95 and a nearly 60 % reduction in error compared to the IRI model. The NET model from A. Smirnov achieves similar quality for altitudes near 500 km. A significant improvement over NET is observed for DMSP, indicating valuable information for enhancing climatological models between 700 and 5,000 km.

In summary, the study highlights the capability of LEO-GNSS observations for reconstructing electron density in the topside ionosphere and plasmasphere, providing valuable insights for improving ionospheric models and understanding variations in electron density at different altitudes.

## 8 Open Research

Swarm GPS observation files, attitude data and orbit information and Langmuir probe data is obtained from `ftp://swarm-diss.eo.esa.int/`. GRACE-FO GPS observation files, attitude, orbits, and inter-satellite electron density is obtained from `ftp://isdcftp.gfz-potsdam.de/grace/`. Sentinel I/II/II GPS observation files, and orbits are obtained from `https://dataspace.copernicus.eu/` Jason-3 GPS observations, orbit, and attitude were provided within the project from AIUB. COSMIC-2 GPS observation files, orbit and attitude was obtained via `https://data.cosmic.ucar.edu/gnss-ro/cosmic2` The required Spire data was provided by ESA within in the frame of an Announcement of Opportunity (project no. 66978). DMSP in situ electron density observation were obtained via `http://cedar.openmadrigal.org` Altimeter TEC is obtained from TU Munic (`https://openadb.dgfi.tum.de/en/products/vertical-total-electron-content/`) Precise GPS orbits are obtained from AIUB (Dach et al., 2020). TEC maps generated from ground based stations were taken from the IGS `ftp://gssc.esa.int/gnss/products/ionex/` and GFZ `ftp://isdcftp.gfz-potsdam.de/gnss/products/iono/`

**Acknowledgments**

This work is part of the DFG HOLMES project, grant number 471275159. We acknowledge the support from Spire Global and the provision of Spire data by ESA in the frame of an Announcement of Opportunity (project no. 66978).

The authors would like to thank Cyril Kobel for computing and providing precise orbits for the Spire satellites.

## References

Arnold, D., Peter, H., Mao, X., Miller, A., & Jäggi, A. (2023). Precise orbit determination of spire nano satellites. *Advances in Space Research*. Retrieved from `https://www.sciencedirect.com/science/article/pii/S0273117723008165` doi: 10.1016/j.asr.2023.10.012

Beyerle, G. (2009). Carrier phase wind-up in gps reflectometry. *GPS Solutions*, *13*(3), 191–198. doi: 10.1007/s10291-008-0112-1

Brack, A., Männel, B., Wickert, J., & Schuh, H. (2021). Operational multi-gnss global ionosphere maps at gfz derived from uncombined code and phase observations. *Radio Science*, *56*(10), e2021RS007337. Retrieved from `https://agupubs.onlinelibrary.wiley.com/doi/abs/10.1029/2021RS007337` (e2021RS007337 2021RS007337) doi:

10.1029/2021RS007337

Cai, C., Liu, Z., Xia, P., & Dai, W. (2013). Cycle slip detection and repair for undifferenced GPS observations under high ionospheric activity. *GPS Solutions*, *17*, 247-260. doi: 10.1007/s10291-012-0275-7

Catapano, F., Buchert, S., Qamili, E., Nilsson, T., Bouffard, J., Siemes, C., ... Stromme, A. (2022). Swarm langmuir probes' data quality validation and future improvements. *Geoscientific Instrumentation, Methods and Data Systems*, *11*(1), 149–162. Retrieved from https://gi.copernicus.org/articles/11/149/2022/ doi: 10.5194/gi-11-149-2022

Chapman, S. (1931, jan). The absorption and dissociative or ionizing effect of monochromatic radiation in an atmosphere on a rotating earth. *Proceedings of the Physical Society*, *43*(1), 26–45. doi: 10.1088/0959-5309/43/1/305

Dach, R., Schaer, S., Arnold, D., Kalarus, M., Prange, L., Stebler, P., ... Jäggi, A. (2020). *CODE final product series for the IGS.* doi: 10.7892/boris.75876.4

DISC. (2017). *Swarm Level 2 TEC product description* (Tech. Rep.). ESA, BGS, DTU, DUT, GFZ, ETH, IPGP, IRF, Leti, UoC, VZLU.

Emmert, J. T., Richmond, A. D., & Drob, D. P. (2010). A computationally compact representation of magnetic-apex and quasi-dipole coordinates with smooth base vectors. *Journal of Geophysical Research: Space Physics*, *115*(A8). Retrieved from https://agupubs.onlinelibrary.wiley.com/doi/abs/10.1029/2010JA015326 doi: https://doi.org/10.1029/2010JA015326

Foelsche, U., & Kirchengast, G. (2002). A simple "geometric" mapping function for the hydrostatic delay at radio frequencies and assessment of its performance. *Geophysical Research Letters*, *29*(10), 111-1-111-4. Retrieved from https://agupubs.onlinelibrary.wiley.com/doi/abs/10.1029/2001GL013744 doi: 10.1029/2001GL013744

Montenbruck, O., & Kroes, R. (2003). In-flight performance analysis of the CHAMP BlackJack GPS Receiver. *GPS Solutions*, *7*, 74-86. doi: 10.1007/s10291-003-0055-5

Montenbruck, O., Schmid, R., Mercier, F., Steigenberger, P., Noll, C., Fatkulin, R., ... Ganeshan, A. (2015). Gnss satellite geometry and attitude models. *Advances in Space Research*, *56*(6), 1015–1029. Retrieved from https://www.sciencedirect.com/science/article/pii/S0273117715004378 doi: 10.1016/j.asr.2015.06.019

Noja, M., Stolle, C., Park, J., & Lühr, H. (2013). Long-term analysis of ionospheric polar patches based on CHAMP TEC data. *Radio Science*, *48*(3), 289-301. Retrieved from https://agupubs.onlinelibrary.wiley.com/doi/abs/10.1002/rds.20033 doi: https://doi.org/10.1002/rds.20033

Nsumei, P., Reinisch, B. W., Huang, X., & Bilitza, D. (2012). New vary-chap profile of the topside ionosphere electron density distribution for use with the iri model and the giro real time data. *Radio Science*, *47*(4). Retrieved from https://agupubs.onlinelibrary.wiley.com/doi/abs/10.1029/2012RS004989 doi: https://doi.org/10.1029/2012RS004989

Pakhotin, I. P., Burchill, J. K., Förster, M., & Lomidze, L. (2022, Jul 12). The Swarm Langmuir probe ion drift, density and effective mass (SLIDEM) product. *Earth, Planets and Space*, *74*(1), 109. Retrieved from https://doi.org/10.1186/s40623-022-01668-5 doi: 10.1186/s40623-022-01668-5

Prol, F., Hoque, M., & Ferreira, A. (2021). Plasmasphere and topside ionosphere reconstruction using metop satellite data during geomagnetic storms. *J. Space Weather Space Clim.*, *11*, 5. Retrieved from https://doi.org/10.1051/swsc/2020076 doi: 10.1051/swsc/2020076

Rawer, K. (1983). Replacement of the present sub-peak plasma density profile by a unique expression. *Advances in space research*, *2*(10), 183-190.

Richmond, A. D. (1995). Ionospheric electrodynamics using magnetic apex coordinates. *Journal of geomagnetism and geoelectricity*, *47*(2), 191–212. doi: 10.5636/jgg.47.191

Ripoll, J.-F., Pierrard, V., Cunningham, G. S., Chu, X., Sorathia, K. A., Hartley, D. P., ... Ukhorskiy, A. Y. (2023). Modeling of the cold electron plasma density for radi-

ation belt physics. *Frontiers in Astronomy and Space Sciences*, *10*. Retrieved from https://www.frontiersin.org/articles/10.3389/fspas.2023.1096595 doi: 10.3389/fspas.2023.1096595

Schaer, S. (2011). *Activities of IGS Bias and Calibration Working Group.* In: Meindl M, Dach R, Jean Y (eds) IGS Technical Report 2011.

Schreiter, L., Stolle, C., Rauberg, J., Kervalishvili, G., van den Ijssel, J., Arnold, D., ... Callegare, A. (2023). Topside ionosphere sounding from the champ, grace, and grace-fo missions. *Radio Science*, *58*(3), e2022RS007552. Retrieved from https://agupubs.onlinelibrary.wiley.com/doi/abs/10.1029/2022RS007552 (e2022RS007552 2022RS007552) doi: 10.1029/2022RS007552

Smirnov, A., Shprits, Y., Prol, F., Lühr, H., Berrendorf, M., Zhelavskaya, I., & Xiong, C. (2023, Jan 24). A novel neural network model of earth's topside ionosphere. *Scientific Reports*, *13*(1), 1303. Retrieved from https://doi.org/10.1038/s41598-023-28034-z doi: 10.1038/s41598-023-28034-z

Truhlik, V., Bilitza, D., & Triskova, L. (2015). Towards better description of solar activity variation in the international reference ionosphere topside ion composition model. *Advances in Space Research*, *55*(8), 2099–2105. Retrieved from https://www.sciencedirect.com/science/article/pii/S027311771400489X (INTERNATIONAL REFERENCE IONOSPHERE AND GLOBAL NAVIGATION SATELLITE SYSTEMS) doi: 10.1016/j.asr.2014.07.033

UCAR. (2019). Ucar cosmic program, 2019: Cosmic-2 data products level 1b podtc2. ucar/ncar - cosmic, access date 2023/03/17.
doi: 10.5065/T353-C093

Wu, J. T., Wu, S. C., Hajj, G. A., Bertiger, W. I., & Lichten, S. M. (1992). Effects of antenna orientation on gps carrier phase. *Astrodynamics 1991; Proceedings of the AAS/AIAA Astrodynamics Conference, Durango, CO, Aug. 19-22, 1991. Pt. 2 (A92-43251 18-13). San Diego, CA, Univelt, Inc., 1992, p. 1647-1660.*.

Yue, X., Schreiner, W. S., Hunt, D. C., Rocken, C., & Kuo, Y.-H. (2011). Quantitative evaluation of the low Earth orbit satellite based slant total electron content determination. *Space Weather*, *9*(9). Retrieved from https://agupubs.onlinelibrary.wiley.com/doi/abs/10.1029/2011SW000687 doi: 10.1029/2011SW000687